applied sciences

MDPI

Article

Near and Far Fields of a Dipole Antenna: A Unified Model

Daniele Funaro [1,2,*], Lorella Fatone [3] and Gianmarco Manzini [2]

1 Dipartimento di Scienze Chimiche e Geologiche, Università di Modena e Reggio Emilia, 41100 Modena, Italy
2 Istituto di Matematica Applicata e Tecnologie Informatiche "E. Magenes", Consiglio Nazionale Delle Ricerche, 27100 Pavia, Italy; gianmarco.manzini@cnr.it
3 Scuola di Scienze e Tecnologie, Polo di Matematica "G. Giachetta", Università di Camerino, 62032 Camerino, Italy; lorella.fatone@unicam.it
* Correspondence: daniele.funaro@unimore.it

Featured Application

The proposed framework enables direct time-domain simulation of electromagnetic emission from antenna devices, including the full near-to-far field transition. The approach is applicable to the design of dipole and monopole antennas, antenna arrays, and other radiating structures for which accurate near-field characterization is critical, and it offers a starting point for numerical tools that do not rely on wave-equation reductions or eigenfunction expansions.

Abstract

The dipole antenna is one of the oldest and most widely used devices in electromagnetic engineering, yet the behavior of its near-field during emission remains only partially captured by classical models. In the source-free region surrounding the arms, the vacuum Maxwell–Heaviside equations provide an insufficient number of configurations to describe the transient through which a bound signal becomes a freely propagating wave. We revisit the model equations, introducing an extended formulation in which an auxiliary velocity field complements the electromagnetic fields. Similarly to plasma physics, the outgoing signal is treated as an electromagnetic fluid carrying a charge density. As the far field is concerned, the resulting system admits an exact family of spherical free-wave solutions that follow the rules of geometrical optics. The near-to-far field transition also acquires a concrete dynamical description, thanks to the introduction of the pseudocharge, which is a charge-like density identified with the divergence of the electric field. In addition, a pressure-like potential, vanishing in the far field, tracks the conversion between bound and radiating energy. The approach is illustrated on a standard dipole antenna through direct numerical simulation of the full coupled system. The results suggest a unified analytical and computational pathway for antenna modeling, with natural extensions to more complex geometries and other radiating devices.

Keywords: dipole antenna; near field; electromagnetic radiation; Maxwell–Heaviside equations; fluid dynamics; geometrical optics; numerical simulation

Academic Editor: Piotr Gas

Received: 13 July 2026
Revised: 5 August 2026
Accepted: 15 August 2026
Published: 21 August 2026

1. Introduction

The dipole antenna has been, for more than a century, one of the central devices of radio engineering, and it continues to serve as the building block for a wide variety of modern radiating structures [1,2]. Contemporary research continues to expand this family of radiating and wavefront-shaping structures, with recent examples including three-dimensionally printed polarization-division metadevices, ultra-wideband Vivaldi antenna arrays, and programmable coding metasurfaces [3–5]. Multi-dipole antenna arrays also find use in biomedical contexts, where the powers and phases of the individual dipoles are optimized to concentrate the electromagnetic energy for localized tumor heating [6,7]. Classical antenna analysis approaches the simple dipole problem through well-established tools. Hertzian multipole expansions, retarded potentials, and numerical methods such as the method of moments (MoM) [8,9] provide predictions of radiation patterns, input impedance, and current distributions on the conductor. These techniques are often built around asymptotic formulae based on the decomposition into divergence-free vector eigenfunctions.

A specific mathematical feature motivates a closer look at the governing equations. In a source-free region, the vacuum Maxwell–Heaviside system requires $\nabla \cdot \mathbf{E} = 0$. However, exact outgoing waves compatible with the rules of geometrical optics [10]—the kind of solutions one would wish to use as idealized carriers of antenna radiation—do not in general satisfy this constraint, as can be verified by direct computations [11–13]. This tension is usually resolved in practice by accepting a small-divergence error that decays faster than the signal itself and is therefore negligible for engineering purposes. From a modeling standpoint, however, it suggests that the source-free vacuum formulation might be more constrained than the physics of antenna radiation requires, and that an extended equation model could remove the problem without altering any empirically established conclusion.

Although the far-field behavior is mathematically not well implemented, engineering design is not very much affected. The near-field region, by contrast, remains conceptually more delicate. In the immediate neighborhood of the arms, the signal retains a strong connection to the feeding geometry, where the circulating current requires that the divergence of the electric field is not zero. A detailed description of the mechanism by which a signal bound to a conductor becomes a radiating wave is the subject of the present work. The scope of this paper is therefore deliberately focused to provide a self-contained field-level description of the near-to-far transition, formulated at the level of the governing equations and illustrated by direct numerical simulation, complementing the existing analytical and computational toolkit and opening a natural path toward the modeling of more complex radiating structures.

The electromagnetic fields $\mathbf{E}$ and $\mathbf{B}$ are coupled to an auxiliary velocity field $\mathbf{V}$ and other scalar quantities. Among the latter, we find a pressure potential p, which can actually be transformed into physical forces—for example, in the study of the radiation pressure of an electromagnetic phenomenon on a material obstacle [14,15]. This mechanical aspect of the model is not merely formal: it underlies experimental techniques such as optical and magnetic tweezers [16,17], in which strongly localized electromagnetic fields trap and manipulate microscopic particles through the forces that they exert. These techniques have been extended to hold and move a broad range of objects, from individual viruses and bacteria to living cells and single biological molecules [18–20]. Because light carries linear and angular momentum, the same fields can also exert torques and drive controlled rotation, so that forces have been used up to the limits of the nanoscale [21–23]. Related force-measurement techniques, including magnetic tweezers, extend this mechanical control to the single-molecule regime, and the breadth of these methods is documented in several reviews [24–27]. Such effects are usually described phenomenologically, whereas the present framework may account for them at the field level, although this is not the subject of this article. This endows the electromagnetic field with a genuine Newtonian character.

Our choice is inspired by the treatment of plasma dynamics in classical electrodynamics [2] and, more broadly, by ideal magnetohydrodynamic models [28–30]. The framework builds upon a longer-running line of work on extended electrodynamic models [13,31,32], to which the present paper contributes with a focused treatment of the dipole antenna problem. Since we have stated that the condition $\nabla \cdot \mathbf{E} = 0$ is too restrictive, we will assume that the electric field can have nonzero divergence even in vacuum. We would then introduce a scalar quantity ρ, called *pseudocharge*, which accompanies the signal emission for its entire evolution. This will be proportional to $\nabla \cdot \mathbf{E}$ and will be treated in the equations as a real moving charge, although there are no effective particles present. Coupling with the Euler equations for fluids also requires the introduction of a *pseudomass* ρ_m, that is, a virtual mass density in the complete absence of massive physical particles. Previous attempts have been made [33,34] regarding the design of an antenna with high directivity. In that case, the model was not fully implemented, and issues related to the stability of the numerical method and the imposition of boundary conditions were not addressed with due care.

It should be stressed that the resulting model is not a numerical method for the Maxwell–Heaviside equations but a distinct system of governing equations, and this has a consequence for the way it is to be validated. Standard Maxwell-based solvers, such as FDTD, finite elements, or the method of moments, assume a divergence-free electric field in source-free regions. A direct comparison between our approach and the more usual ones would contrast different governing equations rather than different approximations, and it would not constitute an equivalent validation. Moreover, the departure from Maxwell persists arbitrarily far from the source. As shown in Section 4, even the free-wave regime retains a nonzero divergence and does not satisfy the standard Maxwell–Heaviside system. The model is therefore assessed against the exact free-wave solutions of the extended system and by direct numerical simulation, rather than by benchmarking against a divergence-free solver.

The rest of this paper is organized as follows: Section 2 presents the mathematical framework, i.e., the extended system of partial differential equations and its covariant derivation starting from a classical stress-energy tensor. Section 3 discusses the famous Hertzian solution simulating an infinitesimal dipole. It is shown that, in proximity of the axis, the wave-fronts depart from the spherical shape. In contrast, Section 4 introduces a family of *free-wave* solutions, consisting of exact mathematical expressions satisfying both the rules of geometrical optics and the extended system of model equations. Section 5 (Materials and Methods) sets up the canonical dipole-antenna problem and describes the numerical discretization of the full system of differential equations. Section 6 reports the numerical experiments based on direct time-domain simulation. Additional comments and considerations are reported in Section 7. Section 8 presents the concluding remarks.

2. The Differential Model

We introduce a system of partial differential equations coupling the electromagnetic fields to an auxiliary velocity field. This will extend the classical Maxwell–Heaviside set of equations for electrodynamics. In order to proceed, let $\mathbf{E}$ and $\mathbf{B}$ denote the electric and magnetic fields, and let $\mathbf{V}$ denote a vector field with the dimension of a velocity. The auxiliary field $\mathbf{V}$ is understood as the local direction along which electromagnetic information is transported; in the simplest cases, it aligns with the Poynting vector $\mathbf{E} \times \mathbf{B}$, but this identification is not assumed a priori, and such arbitrariness is one of the characteristics of the method.

We define the scalar

$$\rho = \nabla \cdot \mathbf{E}, \tag{1}$$

which will be called *pseudocharge*. To be more precise, note that $\epsilon_0 \rho$, where ϵ_0 is the vacuum permittivity, has the dimension of a density of charge per unit of volume. Note that here the electric field is supposed to have the dimension $[M^1 Q^{-1} L^1 T^{-2}]$. Furthermore, let us also introduce the two scalar quantities ρ_m and p. The former has the dimension of a density of mass per unit of volume; the latter can be interpreted either as energy density per unit of volume or as a pressure density per unit of surface. No assumption is made a priori about the sign of ρ, ρ_m, or p. It is appropriate to make a clarification on the physical state of these quantities. They are not intended as new directly measurable observables, and this is not a deficiency of the model. Already, in classical electromagnetism, the divergence $\nabla \cdot \mathbf{E}$ is not a directly accessible local quantity: it is reconstructed from spatial derivatives of the field, and any probe introduced to sample it perturbs the very field being measured. Moreover, ρ and ρ_m are not relativistic invariants. They depend on the choice of the metric space. In particular, in that generated by the phenomenon itself, through the solution of Einstein's equations, ρ vanishes [13,32]. The role of ρ and ρ_m is therefore to complete the field-level description of the electromagnetic phenomenon in a physically consistent way, as the covariant derivation below makes explicit, rather than to name quantities to be measured in isolation.

The full set of model equations reads

$$\frac{\partial \mathbf{E}}{\partial t} = c^2\, \nabla \times \mathbf{B} - \rho\, \mathbf{V}, \qquad \frac{\partial \mathbf{B}}{\partial t} = -\nabla \times \mathbf{E}, \qquad \nabla \cdot \mathbf{B} = 0, \tag{2}$$

$$\rho_m\, \frac{D\mathbf{V}}{Dt} = -\epsilon_0\, \rho\, (\mathbf{E} + \mathbf{V} \times \mathbf{B}) - \nabla p, \qquad \frac{\partial \rho_m}{\partial t} + \nabla \cdot (\rho_m\, \mathbf{V}) = 0, \tag{3}$$

$$\frac{\partial p}{\partial t} = \epsilon_0\, \rho\, \mathbf{E} \cdot \mathbf{V}, \tag{4}$$

where c is the speed of light in vacuum and $D/Dt = \partial_t + \mathbf{V} \cdot \nabla$ denotes the substantial derivative. The first two relations in (2) are the Ampère and Faraday laws, respectively. The source term in Ampère's equation takes the form $\rho\mathbf{V}$. Here, we add the contribution of pseudocharge by treating it as a current, even though there are no real charges in motion. The third relation in (2) is the solenoidal constraint on the magnetic field, consistent with the empirical absence of magnetic monopoles. The first relation in (3) is the Euler momentum balance, which includes a Lorentz-type forcing term; the second is the mass-continuity equation for ρ_m. Equation (4) governs the evolution of the potential p; its form follows from the energy balance, as discussed below. Taking the divergence of the first equation in (2) and using $\nabla \cdot (\nabla \times \mathbf{B}) = 0$ automatically yields the continuity equation

$$\frac{\partial \rho}{\partial t} + \nabla \cdot (\rho\, \mathbf{V}) = 0, \tag{5}$$

which expresses the conservation of pseudocharge. Instead, taking the scalar product of the first equation in (2) with $\epsilon_0\, \mathbf{E}$ and of the second with $\epsilon_0\, c^2\, \mathbf{B}$, and combining the results, yields the energy relation

$$\frac{\partial \mathcal{E}}{\partial t} = -\epsilon_0 \Big(c^2\, \nabla \cdot (\mathbf{E} \times \mathbf{B}) + \rho\, \mathbf{E} \cdot \mathbf{V} \Big), \tag{6}$$

where $\mathcal{E} = \frac{1}{2}\, \epsilon_0\, (|\mathbf{E}|^2 + |c\mathbf{B}|^2)$ is the electromagnetic energy density. The term $\nabla \cdot (\mathbf{E} \times \mathbf{B})$ is the divergence of the Poynting vector. The additional term $\epsilon_0 \rho\, \mathbf{E} \cdot \mathbf{V}$ represents a sort of exchange between electromagnetic and mechanical forces. It disappears at the far field, bringing the discussion back to more classical canons.

In order to justify that the system (2)–(4) is physically acceptable, we show its derivation starting from a classical stress-energy tensor. Working with four vectors in the system of coordinates $x^\alpha = (ct, x, y, z)$, with a space-time metric $g_{\alpha\beta}$ of signature $(+,-,-,-)$, let $F_{\alpha\beta}$

https://doi.org/10.3390/app16168334

denote the classical electromagnetic field tensor [35,36]. The electromagnetic stress-energy tensor takes the standard form

$$U_{\alpha\beta} = -g^{\gamma\delta} F_{\alpha\gamma} F_{\beta\delta} + \tfrac{1}{4} g_{\alpha\beta} F_{\gamma\delta} F^{\gamma\delta}. \tag{7}$$

Introducing the velocity four-vector $V_\alpha = (c, -\mathbf{V})$, $V^\alpha = g^{\alpha\beta} V_\beta$, and the corresponding tensor

$$M_{\alpha\beta} = \rho_m V_\alpha V_\beta - g_{\alpha\beta}\, p, \tag{8}$$

with the form of a mass tensor recalling a dust of particles for a perfect fluid, we set

$$T_{\alpha\beta} = M_{\alpha\beta} - \epsilon_0 U_{\alpha\beta}. \tag{9}$$

The covariant version of the model equations is then obtained by computing the four-vector divergence

$$\nabla_\beta T^{\alpha\beta} = 0, \qquad \alpha = 0, 1, 2, 3. \tag{10}$$

We check this in the Minkowski metric, with $\nabla_\beta = (\partial_t / c, \nabla)$. For $\alpha = 0$, (10) reads

$$\begin{aligned} c\left[\frac{\partial \rho_m}{\partial t} + \nabla \cdot (\rho_m \mathbf{V})\right] - \frac{1}{c}\left[\frac{\partial p}{\partial t} - \epsilon_0\, \rho\, \mathbf{E} \cdot \mathbf{V}\right] & \\ - \left[\frac{\epsilon_0}{c}\frac{\partial \mathcal{E}}{\partial t} + \epsilon_0\, c\, \nabla \cdot (\mathbf{E} \times \mathbf{B}) + \frac{\epsilon_0}{c}\, \rho\, \mathbf{E} \cdot \mathbf{V}\right] &= 0, \end{aligned} \tag{11}$$

where we have added and subtracted the term $(\epsilon_0 / c) \rho \mathbf{E} \cdot \mathbf{V}$. Relation (11) is consistent with the mass continuity equation in (3), the pressure Equation (4), and the energy relation (6). The components $\alpha = 1, 2, 3$ of (10) combine into the vector relation

$$\begin{aligned} &\left[-\epsilon_0\left(\frac{\partial \mathbf{B}}{\partial t} + \nabla \times \mathbf{E}\right) \times \mathbf{E}\right] + \left[\epsilon_0\left(\frac{\partial \mathbf{E}}{\partial t} - c^2\, \nabla \times \mathbf{B} + \rho\, \mathbf{V}\right) \times \mathbf{B}\right] \\ &\qquad - \left[\epsilon_0\, c^2\, (\nabla \cdot \mathbf{B})\, \mathbf{B}\right] - \left[\rho_m \frac{D\mathbf{V}}{Dt} + \epsilon_0\, \rho\, (\mathbf{E} + \mathbf{V} \times \mathbf{B}) + \nabla p\right] = 0, \end{aligned} \tag{12}$$

where we have added and subtracted the term $\epsilon_0 \rho \mathbf{V} \times \mathbf{B}$. This is consistent with (2) and with the Euler equation in (3).

We now discuss some special cases. Setting $p = 0$, $\rho_m = 0$, and $\rho = 0$ in (1) and (2)–(4), we recover the classical vacuum system

$$\frac{\partial \mathbf{E}}{\partial t} = c^2\, \nabla \times \mathbf{B}, \qquad \frac{\partial \mathbf{B}}{\partial t} = -\nabla \times \mathbf{E}, \qquad \nabla \cdot \mathbf{E} = 0, \qquad \nabla \cdot \mathbf{B} = 0, \tag{13}$$

in the form customarily referred to as the Maxwell–Heaviside equations. The system (13) is, strictly, the reformulation proposed by O. Heaviside [37] of J. C. Maxwell's original system (pp. 161–175, 281–512, [38]) and [39], but commonly attributed to Maxwell.

A second simplification is of particular interest. Setting $p = 0$ and $\rho_m = 0$ but allowing $\rho \neq 0$, the system (2)–(4) reduces to

$$\frac{\partial \mathbf{E}}{\partial t} = c^2\, \nabla \times \mathbf{B} - \rho\, \mathbf{V}, \qquad \frac{\partial \mathbf{B}}{\partial t} = -\nabla \times \mathbf{E}, \qquad \mathbf{E} + \mathbf{V} \times \mathbf{B} = \mathbf{0}, \qquad \nabla \cdot \mathbf{B} = 0. \tag{14}$$

Following [31,32], we refer to the solutions of (14) as *free waves*. They collect all electromagnetic phenomena that develop according to the rules of geometrical optics. We provide further explanations for this choice. The algebraic constraint $\mathbf{E} + \mathbf{V} \times \mathbf{B} = \mathbf{0}$ in (14) implies that $\mathbf{E}$ is orthogonal to both $\mathbf{B}$ and $\mathbf{V}$ pointwise. The vector field $\mathbf{V}$ turns out to be constant in magnitude, with a norm equal to the speed of light: $|\mathbf{V}| = c$. As a consequence, it is perfectly lined up with the Poynting's vector. If, for example, $\mathbf{V} = \nabla\Psi$ (that is, the velocity field is a gradient), the relation $|\nabla\Psi| = c$ corresponds to the stationary *eikonal equation* [10], which rules the propagation of fronts in classical optics (this is $V^\alpha V_\alpha = 0$ in the framework of general relativity). In this regime, since the term $\mathbf{E} \cdot \mathbf{V}$ vanishes identically, the energy balance in (6) reduces to the standard Poynting theorem. The classical relation $|\mathbf{E}| = |c\mathbf{B}|$ (connected to the impedance of free space) also follows from the equations. Free waves thus describe electromagnetic phenomena propagating transversally at the speed of light along rays determined by $\mathbf{V}$, in consistency with geometrical optics. As a final remark, we note that Equation (14) is Lorentz-invariant [31,32]. This also includes the equation $\mathbf{E} + \mathbf{V} \times \mathbf{B} = \mathbf{0}$, making the concept of a free wave observer-independent.

3. Hertzian Waves

In the study of the propagation of electromagnetic signals, the corresponding wave equations are usually derived. This is very easy in vacuum using the equations in (13). A little calculus allows us to recover the following vector wave equation for the electric field:

$$\frac{\partial^2 \mathbf{E}}{\partial t^2} = c^2 \Delta \mathbf{E}, \qquad\qquad \nabla \cdot \mathbf{E} = 0. \tag{15}$$

The same is valid for the magnetic field. For example, the coupling with $\mathbf{B}$ can occur via boundary conditions. Note that the divergence relation must be maintained, so we find ourselves with four equations with three unknowns (the three components of $\mathbf{E}$). Although it is better to be suspicious about problems where the number of relationships is greater than the unknowns, there are sometimes magic solutions where all requests are fulfilled. This is the famous Hertz's solution (see [40,41], or [10], p. 81), which satisfies both the vector wave equation and the divergence constraint. It is obtained from eigenfunctions of the vector Laplacian in spherical coordinates (r, θ, ϕ), with $r \geq 0$, $0 \leq \theta \leq \pi$, $0 \leq \phi < 2\pi$. For symmetry reasons, there is no dependency on ϕ, but the functions explicitly depend on r (involving Bessel spherical functions) and θ (involving Legendre polynomials). A representative example, for a single monochromatic mode of frequency $\omega/2\pi$, is

$$\begin{aligned}\mathbf{E} = \Bigg(&\frac{2\cos\theta}{r^2}\Big(\frac{\sin\omega(ct - r)}{r} + \omega\cos\omega(ct - r)\Big), \\ &\frac{\sin\theta}{r}\Big(\frac{\omega\cos\omega(ct - r)}{r} + \Big(\frac{1}{r^2} - \omega^2\Big)\sin\omega(ct - r)\Big),\ 0\Bigg).\end{aligned} \tag{16}$$

The field $\mathbf{B}$ (not reported here) has only the component relative to the angle ϕ. At a given time, the lines of force of this configuration are shown—for instance in [42], p. 340. They seem to fit perfectly with the infinitesimal dipole antenna problem, where the arms collapse into a single point. However, this approach reveals several inconsistencies, as discussed below.

The fields travel radially at the speed of light departing from the origin. The azimuth intensity behaves like $\sin\theta$, as is usually observed in this kind of radiation (see also (18)). Note that the electric field also contains a radial component, which means that it is not perfectly transverse to the direction of propagation. For any fixed r, a direct analysis shows that the non-radial component prevails on the radial one when approaching the vertical axis (i.e., $\theta = 0$ or $\theta = \pi$). This implies that the shape of the wave-fronts, or more exactly the envelope of the lines of force, is not a sphere. Although information at some distance from the source appears to spread along concentric spheres, the overall behavior is different from a topological viewpoint. Indeed, in order to keep the condition

$\nabla \cdot \mathbf{E} = 0$, the wave-fronts bend in proximity of the vertical axis. It is easy to realize that, in 3D, these are toroidal surfaces. Technically, Hertzian waves are not spherical waves. We see no possibility of recognizing any kind of Huygens principle in this behavior, as the rules of geometrical optics are disregarded. A discussion on the limits of geometrical optics is provided for example in (Section 3.1.4, [10]), It is important not to confuse (as often happens) the envelope of the lines of force with the contour lines of the intensity of the electric field. Graphically, their behavior is similar, but their meaning is completely different.

Other solutions, related to so-called multipole radiation, are obtained by summing up more eigenfunctions. In [11], a suitable expansion is found with the aim of satisfying specific boundary constraints and improving the behavior of Poynting's vectors when r is large. However, inconsistent behavior persists in a layer near the vertical axis, as well as near the origin [12]. An alternative approach followed by many authors is to introduce the potentials

$$\mathbf{B} = \frac{1}{c}(\nabla \times \mathbf{A}), \qquad\qquad \mathbf{E} = -\frac{1}{c}\frac{\partial \mathbf{A}}{\partial t} - \nabla\Phi. \tag{17}$$

In this way, the two equations $\partial\mathbf{B}/\partial t = -\nabla \times \mathbf{E}$ and $\nabla \cdot \mathbf{B} = 0$ are automatically satisfied. Without going into technical details, the potential-based approach does not eliminate the problems seen so far. The solutions obtained by the so-called "retarded potential" suffer from the same anomalies.

Since the behavior discussed here can be explained with the help of slight adjustments, while remaining within the so-called "limits of the model", we could simply stop our analysis here with the trivial conclusion that the Maxwell–Heaviside model is imperfect. However, as we will see in this article, things can be drastically improved by implementing the right corrections. As extensively documented in [13], the Maxwell–Heaviside model imposes too many constraints (more equations than unknowns), making the solution space excessively small and insufficient to describe even the simplest applications. The main argument is that the relation $\nabla \cdot \mathbf{E} = 0$ cannot be enforced, for example, in the vacuum space between two (non-pointwise) bodies whose charge varies with time (or they are in motion, relative to each other). This is exactly what happens in the case of the antenna arms subjected to alternating negative and positive differences of potential. Conversely, there are no problems regarding the equation $\nabla \cdot \mathbf{B} = 0$. This means that we could also talk about density of charge in regions of the space where physical charges are missing. In this case, we say that we are in the presence of pseudocharge.

In Figure 1, we provide three examples where pseudocharge must be present: The first one is a spherical wave (or any other shape topologically isomorphic). Electromagnetic fields (orthogonal to each other) propagate along the radial direction and lay on the local tangent plane of the surface. As they move away from the central source, they decrease in intensity in accordance with energy conservation arguments. As mathematically shown in [13], there is no chance to enforce the condition $\nabla \cdot \mathbf{E} = 0$, regardless of the arrangement of the fields. A wave like this is almost entirely "made" of pseudocharge. A similar situation occurs for the case of plane parallel fronts (central picture in Figure 1). We can arrange the magnetic field in such a way as to satisfy $\nabla \cdot \mathbf{B} = 0$, but there is no hope to do the same for the electric field. The only acceptable solutions in this case are plane waves of infinite transverse extent, which clearly do not exist in nature. This certifies the impossibility of modeling *photons* using the classical electrodynamics equations. The third example in Figure 1 shows the distribution of the electric field outside a dielectric body that changes its charge. For symmetry reasons, if the body is spherical, there is no production of magnetic field. It is easy to prove that the equations in (15) cannot hold at the same time [43]. For instance, $\mathbf{E} = (f(t)/r^2, 0, 0)$, where f is any given function, is divergence-free but does not solve the wave equation. Conversely, solutions of the wave equation cannot be divergenceless. The only way out of this dilemma is to hypothesize the presence of time-dependent pseudocharge around the dielectric. Details are available in [13]. The study of bodies that emit longitudinal waves (such as the last one mentioned above) has emerged since the time of N. Tesla's experiments with high-voltage coils [44,45]. The modeling of these radiations remains a topic to be fully investigated.

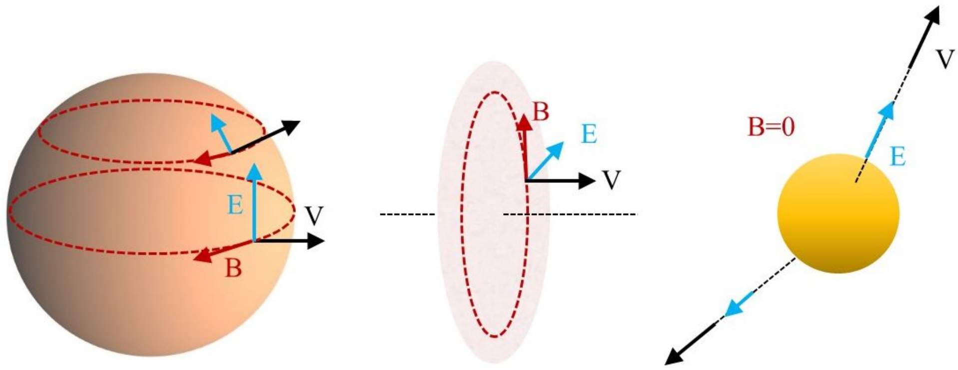

Figure 1. Three examples of electromagnetic emissions that cannot satisfy the condition $\nabla \cdot \mathbf{E} = 0$: (**left**) a spherical wave carrying a transverse signal; (**centre**) a train of plane wave-fronts of finite transverse extent; (**right**) a purely longitudinal exterior field from a spherical source whose charge varies in time.

4. Other Exact Solutions: Free Waves

Let us return to the first case shown in Figure 1 and provide a classic example of spherical wave, satisfying the rules of geometric optics (the Huygens principle, for instance). We already know that it is essential to reject the hypothesis of zero divergence as far as the electric field is concerned. We have

$$\mathbf{E} = \left(0,\ \frac{\sin\theta}{r}\sin\omega(ct-r),\ 0\right), \qquad \mathbf{B} = \left(0,\ 0,\ \frac{\sin\theta}{cr}\sin\omega(ct-r)\right). \tag{18}$$

This displacement is reported in almost all textbooks on electrodynamics and antenna design. Unfortunately, we have $\nabla \cdot \mathbf{E} \neq 0$, so the full set of Maxwell–Heaviside equations is not fulfilled. The decay of the divergence as r tends to infinity is like $1/r^2$, i.e., it fades faster than the signal. This quantity can therefore be neglected in applications. Similarly, it can be verified that $\mathbf{E}$ does not satisfy the wave equation. One usually falls into the following trap: the second component of $\mathbf{E}$ satisfies the **scalar** wave equation. However, we are dealing with vectors in spherical coordinates. The Laplacian of a vector is not the Laplacian of its components in this case. Therefore, the expression in (18) cannot be a solution of the Maxwell–Heaviside model in vacuum.

If we do not take into serious consideration the presence of pseudocharge distributed within the wave (with positive and negative values compensating each other), any attempt is doomed to fail. This brings us to the model (14), which allows ρ to be different from zero. By defining $\mathbf{V} = (c, 0, 0)$, the displacement (18) satisfies the full set of equations. The pseudocharge multiplied by $\mathbf{V}$ becomes the current term in Ampère's equation. The electromagnetic fields are orthogonal to each other and transverse to the spherical front. Poynting's vector has the same direction as $\mathbf{V}$. Moreover, we have the eikonal equation $|\nabla\Psi| = c$, with $\Psi = cr$. The relation $\mathbf{E} + \mathbf{V} \times \mathbf{B} = 0$ now becomes a geometrical constraint that confirms the orthogonality of the triplet $\mathbf{E}, \mathbf{B}, \mathbf{V}$ and guarantees the well-known condition $|\mathbf{E}| = |c\mathbf{B}|$, which can be related to the *impedance of the free space* (about 377 Ω). Even having $\rho \neq 0$, the principle of conservation of charge is preserved. In fact, the continuity Equation (5) guarantees the conservation of pseudocharge.

The expression in (18) is a particular case of the more general form

$$\mathbf{E} = \left(0,\ \frac{f(\theta)}{r} g(ct-r),\ 0\right), \qquad \mathbf{B} = \left(0,\ 0,\ \frac{f(\theta)}{cr} g(ct-r)\right), \tag{19}$$

where f and g are arbitrary functions. With $\mathbf{V} = (c, 0, 0)$ this also solves the system (14). We are therefore in the presence of spherical waves where we can freely modulate the behavior in both the azimuthal and radial directions. This freedom is not accessible in the context of Hertzian waves, where a combination of eigenfunctions constrains the transverse and radial behavior, thus providing a rather limited number of solutions (from the dipole we move directly to the quadripole, without all the nuances of the intermediate cases). Within the context of (19), the only way to get a solution satisfying $\rho = 0$ is to impose $f(\theta) = 1/\sin\theta$, causing a singularity to occur along the vertical axis. Clearly, this hypothesis is inapplicable. Finally, we have already stated that the 3D vector wave equation is not available now. However, by denoting by u the θ-component of the electric field (or the ϕ-component of the magnetic field), we get

$$\frac{\partial^2 (ru)}{\partial t^2} = c^2 \frac{\partial^2 (ru)}{\partial r^2}, \tag{20}$$

which is a 1D scalar wave equation where u is shifting along the axis individuated by $\mathbf{V}$. This is true independently of f and g. The above considerations further strengthen the approach that we are following. The model (14) also allows us to introduce photons as actual portions of plane electromagnetic waves, without resorting to any approximations. As described in [31,32], this opens the way to the interpretation of quantum mechanics in classical terms, although this is a topic that we will not address here.

Note that a sort of wave equation is hidden in formulation (14). In fact, assuming that Lorenz's gauge holds,

$$\frac{\partial \Phi}{\partial t} + c\, \nabla \cdot \mathbf{A} = 0, \tag{21}$$

we get

$$c\left(\frac{\partial \mathbf{A}}{\partial t} + c^2 \Delta \mathbf{A}\right) = \left(\frac{\partial \Phi}{\partial t} + c^2 \Delta \Phi\right)\mathbf{V}. \tag{22}$$

In the Maxwell–Heaviside model, the two terms are both zero—a condition that is not necessarily imposed in our case. Note also that Hertzian solutions are built with the assumption that $\mathbf{A}$ is lined up with the z-axis, which is not the path that we are following here, where we instead have $c\mathbf{A} = \Phi\mathbf{V}$ (i.e., $\mathbf{A}$ is lined up with $\mathbf{V}$), a condition that looks more physical.

When free waves meet an obstacle, it is necessary to resort to the most complete model (2)–(3). Note that we have not removed the Hertzian waves ($\rho = 0$) from the panorama but have embedded them in a larger space. Thus, even in the framework of simple applications, the assumption $\rho \neq 0$ is not just a theoretical trick but a real necessity. We therefore invite the reader to accept possible explanations regarding the operating mechanism of antennas in the light of a solid theory in which non-solenoid electric fields are possible even in a vacuum.

5. Materials & Methods

We are ready to deal with the case of a signal radiating from a realistic dipole. Let us remember that this problem has been around for decades without yet having found a convincing solution. The study of the previous section teaches us how to obtain perfect spherical wave-fronts (or similar isomorphic shapes) without any approximation. These are useful for describing waves traveling in the far field. The idea now is to solve the full set of Equations (2)–(3), subjected to suitable boundary conditions that are imposed at the arms of the antenna (the so-called "feeding"). The study is carried out in the cylindrical coordinates system (r, ϕ, z), $r \geq 0$, $0 \leq \phi < 2\pi$, $\forall z$. We assume that there is no dependency on the variable ϕ. The vector fields will take the special form $\mathbf{E} = (E_1, 0, E_3)$, $\mathbf{B} = (0, B_2, 0)$, $\mathbf{V} = (V_1, 0, V_3)$. Therefore, with the addition of the scalars p and ρ_m, we have seven unknowns, namely, $E_1, E_3, B_2, V_1, V_3, p$, and ρ_m.

An initial velocity field $\mathbf{V}_{\text{init}}$ is provided. This is specified later on (see (33)). The other initial quantities are set to zero (the antenna is off). They will change in time through the imposition of the boundary constraints along the antenna arms and by assuming that the signal decays to zero at the far field. Note that $\mathbf{V}$ does not have to be zero at a distance but must instead have a norm equal to c, since it is responsible for transferring information at the speed of light. This observation is one of the key points of our approach, which clearly distinguishes between the message actually conveyed and the way in which it is conveyed. This distinction is not present in the Maxwell–Heaviside model. Note also that $|\mathbf{V}|$ is generally equal to c only for free waves, so we expect that in the near field $\mathbf{V}_{\text{init}}$ will change with time. This should not be surprising since, as reiterated in [13], there are numerous explicit examples showing that, even when solving the wave Equation (15), information can be carried at speeds other than that of light. For example, there are electromagnetic waves that rotate inside cylinders or toroids, where the velocity varies depending on the distance from the center of rotation. In other words, the presence of the constant c in the equations does not guarantee, even in the simplest cases, that the signal transfer must occur at the speed of light. Let us also observe that the relation $\nabla \cdot \mathbf{V} = 0$ is not requested.

Based on the assumptions on the fields, we can start by computing the divergence:

$$\rho = \nabla \cdot \mathbf{E} = \frac{\partial E_1}{\partial r} + \frac{E_1}{r} + \frac{\partial E_3}{\partial z}. \tag{23}$$

Going ahead, we can update p according to (4):

$$\frac{\partial p}{\partial t} = \epsilon_0 \rho\, \mathbf{E} \cdot \mathbf{V} = \epsilon_0 \rho\, (E_1 V_1 + E_3 V_3). \tag{24}$$

For this, we can use $\mathbf{V}_{\text{init}}$ and the values of p on the antenna, which will be made explicit later. Then is the turn of Faraday's equation:

$$\left(0,\, \frac{\partial B_2}{\partial t},\, 0\right) = \frac{\partial \mathbf{B}}{\partial t} = -\nabla \times \mathbf{E} = \left(0,\, \frac{\partial E_3}{\partial r} - \frac{\partial E_1}{\partial z},\, 0\right), \tag{25}$$

followed by Ampère's law for the pseudocharge:

$$\begin{aligned} \left(\frac{\partial E_1}{\partial t},\, 0,\, \frac{\partial E_3}{\partial t}\right) &= \frac{\partial \mathbf{E}}{\partial t} = c^2\, \nabla \times \mathbf{B} - \rho \mathbf{V} \\ &= \left(-c^2 \frac{\partial B_2}{\partial z} - \rho V_1,\, 0,\, c^2\left(\frac{\partial B_2}{\partial r} + \frac{B_2}{r}\right) - \rho V_3\right). \end{aligned} \tag{26}$$

We proceed with Euler's equation:

$$\begin{aligned} \left(\frac{\partial(\rho_m V_1)}{\partial t},\, 0,\, \frac{\partial(\rho_m V_3)}{\partial t}\right) &= \frac{\partial(\rho_m \mathbf{V})}{\partial t} \\ = -(\nabla \cdot \mathbf{V})(\rho_m \mathbf{V}) - (\mathbf{V} \cdot \nabla)(\rho_m \mathbf{V}) &- \epsilon_0 \rho\, (\mathbf{E} + \mathbf{V} \times \mathbf{B}) - \nabla p \\ = -\left(\frac{\partial V_1}{\partial r} + \frac{V_1}{r} + \frac{\partial V_3}{\partial z}\right) &\left(\rho_m V_1,\, 0,\, \rho_m V_3\right) \\ -\left(V_1 \frac{\partial(\rho_m V_1)}{\partial r} + V_3 \frac{\partial(\rho_m V_1)}{\partial z},\, 0,\, V_1 \frac{\partial(\rho_m V_3)}{\partial r} + V_3 \frac{\partial(\rho_m V_3)}{\partial z}\right) & \end{aligned}$$

$$-\epsilon_0\rho\Big(E_1 - V_3B_2,\ 0,\ E_3 + V_1B_2\Big) - \left(\frac{\partial p}{\partial r},\ 0,\ \frac{\partial p}{\partial z}\right). \tag{27}$$

Here, we used the continuity equation for ρ_m in order to write

$$\begin{aligned}\frac{\partial(\rho_m\mathbf{V})}{\partial t} &= \frac{D(\rho_m\mathbf{V})}{Dt} - (\mathbf{V}\cdot\nabla)(\rho_m\mathbf{V}) = \frac{D\rho_m}{Dt}\,\mathbf{V} + \rho_m\frac{D\mathbf{V}}{Dt} - (\mathbf{V}\cdot\nabla)(\rho_m\mathbf{V})\\ &= \left(\frac{\partial\rho_m}{\partial t} + \nabla\cdot(\rho_m\,\mathbf{V}) - \rho_m\nabla\cdot\mathbf{V}\right)\mathbf{V} + \rho_m\frac{D\mathbf{V}}{Dt} - (\mathbf{V}\cdot\nabla)(\rho_m\mathbf{V})\\ &= -(\nabla\cdot\mathbf{V})(\rho_m\mathbf{V}) - (\mathbf{V}\cdot\nabla)(\rho_m\mathbf{V}) - \epsilon_0\rho(\mathbf{E}+\mathbf{V}\times\mathbf{B}) - \nabla p. \end{aligned} \tag{28}$$

In this way, on the right-hand side, we get a relation for the unknown $\rho_m\mathbf{V}$ instead of $\mathbf{V}$. The reason for this choice lies in the fact that, in the $\rho_m D\mathbf{V}/Dt$ formulation, ρ_m can be zero without $\mathbf{V}$ being zero, making the calculation of this latter vector impossible. If we consider $D(\rho_m\mathbf{V})/Dt$ instead, the quantity $\rho_m\mathbf{V}$ can vanish even if $\mathbf{V}\neq 0$, avoiding divisions by zero. Thus, if $|\rho_m|$ is sufficiently small, $\mathbf{V}$ is left unchanged. As a matter of fact, free waves are characterized by having $\rho_m = 0$ and $p = 0$; however, $\mathbf{V}$ must not vanish, since it satisfies $|\mathbf{V}| = c$. Troubles of this type have also emerged in the study of the scattering of electromagnetic waves in the presence of an obstacle [14,15], where the model was slightly different from that considered here. Finally, before starting the cycle again, we use the continuity equation for the mass

$$\frac{\partial\rho_m}{\partial t} = -\nabla\cdot(\rho_m\,\mathbf{V}) = -\left(\frac{\partial(\rho_m V_1)}{\partial r} + \frac{\rho_m V_1}{r} + \frac{\partial(\rho_m V_3)}{\partial z}\right). \tag{29}$$

The new value of $\mathbf{V}$ is recovered by the division $(\rho_m\mathbf{V})/\rho_m$, provided these two terms are not too small.

The next task is to propose the boundary constraints. The emitting device is going to be the segment $[-d/2, d/2]$ in the direction of the vertical axis. It has a very small gap at the origin, and the two arms are supplied by two independent conducting wires. It is customary to assume that the current I at the ends of the antenna is zero. For $|z| > d/2$, the signal is supposed to be zero. The electromotive force turns out to be proportional to I along the arms, and it depends on the resistance R of the supplying wires. It takes opposite values near the origin, showing a discontinuity for $z = 0$. The electric field thus generated is more intense in the small gap between the two conductors. Note that our device is not infinitesimal. The following is the expression that we suggest for the vertical component E_3 of the electric field:

$$f(t,z) = \sin(2\pi ct/\lambda)\frac{\sin\big(\pi(d-2|z|)/\lambda\big)}{\sin(\pi d/\lambda)}, \qquad |z|\le d/2, \quad t\ge 0, \tag{30}$$

where λ is the wavelength of the feeding signal and $\nu = c/\lambda$ is its frequency. This assumption is rather standard [2]. The function f in (30) satisfies the one-dimensional wave equation

$$\frac{\partial f}{\partial t} = -c\,\mathrm{sign}(z)\,\frac{\partial f}{\partial z} \quad\Longrightarrow\quad \frac{\partial^2 f}{\partial t^2} = c^2\,\frac{\partial^2 f}{\partial z^2}, \tag{31}$$

consistent with the assumption that the current in the conductor flows at the speed of light. For feeding signals of the form (30), different values of the ratio λ/d correspond to different operating regimes of the antenna. The case $\lambda = 2d$ corresponds to the so-called quarter-wave dipole, in which each arm has length $d/2 = \lambda/4$; this is the configuration most commonly used in practice. The case $\lambda = d$ is excluded because the denominator in (30) vanishes. At this frequency, the second harmonic reflects back from the endpoints to the feed point and the antenna does not radiate. Further cases of interest include $\lambda = 2d/3$, the third harmonic, and $\lambda = 4d/5$, which yields a pattern with marked directionality in the $z = 0$ plane.

On the z-axis, the electric component E_1 vanishes by axial symmetry. As far as B_2 is concerned, more investigation is needed. Prescribing E_3 as the feeding signal, and simultaneously enforcing $B_2 = 0$ on the arms, imposes both the incoming and the outgoing characteristic of the hyperbolic system, introducing inconsistency (see the observations in Section 7). We may therefore replace the condition $B_2 = 0$ on the arms by the *impedance-type* relation

$$B_2 = \frac{\tau}{c}\, E_3, \qquad |z| \le d/2, \quad r = 0, \tag{32}$$

where τ is a dimensionless coefficient with $|\tau| < 1$. The limit $|\tau| \to 1$ corresponds to perfect matching to an outgoing cylindrical wave. The characteristic variable $E_3 - \mathrm{sgn}(\tau)\, c\, B_2$ vanishes on the boundary, and the wave leaves the antenna without reflection. The limit $\tau = 0$ recovers the classical perfect-electric-conductor condition $B_2 = 0$, which is well posed only in the presence of additional dissipative mechanisms that absorb the otherwise reflected characteristic. Intermediate values $0 < |\tau| < 1$ represent a partially reflecting but well-posed boundary, consistent with a conductor of finite surface impedance. The sign of τ is fixed by the orientation of the reference frame so that (32) corresponds to an outgoing rather than an incoming characteristic. From the standpoint of hyperbolic PDE theory, the case $|\tau| \neq 1$ corresponds to a *contact discontinuity* [46]. These situations are classically smeared by artificial viscosity, which resolves the discontinuity at the price of dissipation.

The velocity field is initialized with magnitude c at every point. Explicitly,

$$\mathbf{V}_{\mathrm{init}} = \begin{cases} \left(\dfrac{c\, r}{\sqrt{r^2 + (z - d/2)^2}},\ 0,\ \dfrac{c\,(z - d/2)}{\sqrt{r^2 + (z - d/2)^2}} \right), & z > d/2, \\ (c,\ 0,\ 0), & -d/2 \le z \le d/2, \\ \left(\dfrac{c\, r}{\sqrt{r^2 + (z + d/2)^2}},\ 0,\ \dfrac{c\,(z + d/2)}{\sqrt{r^2 + (z + d/2)^2}} \right), & z < -d/2. \end{cases} \tag{33}$$

This is illustrated on the left-hand side of Figure 2. This initial guess is made based on what is expected to be the displacement of the light rays. Later, the velocity field changes periodically over time, without stabilizing, and a snapshot is visible on the right-hand side of Figure 2.

The pseudocharge $\rho = \nabla \cdot \mathbf{E}$, defined in (23), is nonzero both inside the antenna arms, where the current flows, and in the vacuum region surrounding them, where the field configuration near the time-varying source cannot be divergence-free. Along the antenna arms, the initial velocity field (33) takes the radial form $\mathbf{V} = (c, 0, 0)$, while the electric field is purely axial, with $E_1 = 0$ and E_3 prescribed by the feeding signal (30). Consequently, $\mathbf{E} \cdot \mathbf{V}$ vanishes along the arms and, according to Equation (24), it is consistent to impose $p = 0$. Slightly away from the arms, the orthogonality of $\mathbf{E}$ and $\mathbf{V}$ is partially broken, $\mathbf{E} \cdot \mathbf{V}$ is generally nonzero, and the pressure p evolves accordingly. The pressure-like potential tracks the exchange between bound and radiating energy during the transient, and this is the mechanism by which the extended framework accommodates the non-transversal character of the field in the immediate neighborhood of the emitting structure.

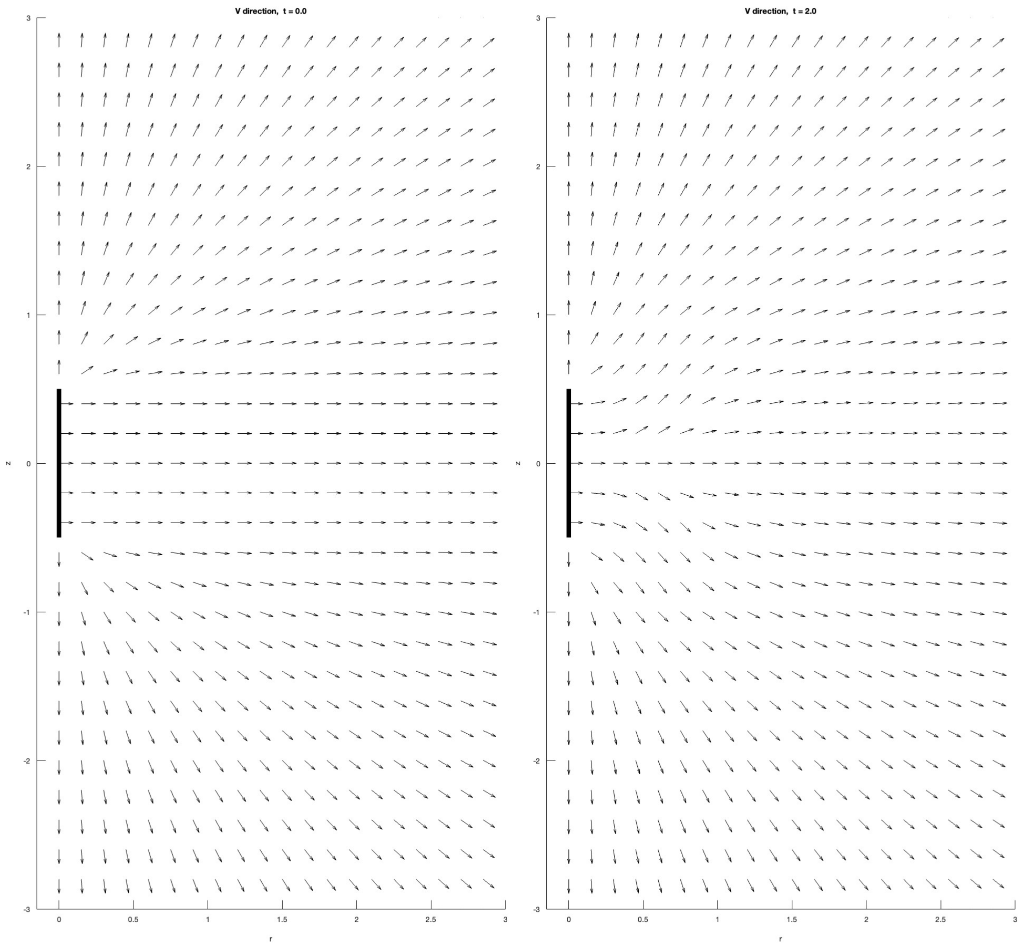

Figure 2. Initial velocity field $\mathbf{V}_{\text{init}}$ defined in (33) (**left**) and velocity field $\mathbf{V}$ at $t = 2$ (**right**), following the dynamics of the Euler equation.

As far as the pseudomass density is concerned, we assume that on the feeding antenna is proportional to the absolute value of the pseudocharge density, namely,

$$\rho_m = M_q \, \epsilon_0 \, |\rho|. \tag{34}$$

where M_q is a suitable constant (see the comments in Section 7) that has the dimensions of mass divided by charge. A rough justification for this relationship is that, in the presence of an accumulation of charges, a corresponding concentration of masses occurs in a proportional manner. Note that ρ and ρ_m have a behavior described by the derivative of the function in (30) and, therefore, exhibit a discontinuity at the antenna endpoints. Inside the computational domain, the pseudomass evolves according to the conservation law (29), while the relation (34) only prescribes the value injected at the source. The absolute value $|\rho|$ guarantees that ρ_m is non-negative, consistent with its interpretation as a mass-like density. Similar constitutive relations were already considered in the framework of the extended electromagnetic model developed in [31,32], where the pseudomass was related to the pseudocharge through a proportionality constant. In the present work, however, the relation is used exclusively to set up the boundary data.

The expected qualitative behavior can be summarized as follows: In the immediate neighborhood of the arms, the electric and magnetic fields are not yet mutually in phase. As we move from the arms, the electromagnetic energy released by the feeding signal is partially stored in the pressure-like potential p. As the signal moves far away from the antenna, p decreases, and the orthogonality of $(\mathbf{E}, \mathbf{B}, \mathbf{V})$ is progressively restored. At this point, the transient period is finished, and the fields approach a free-wave configuration

https://doi.org/10.3390/app16168334

in which the following relations are satisfied: p and ρ_m vanish, $|\mathbf{V}| \to c$, $\mathbf{V}$ aligns with the Poynting vector, and $|\mathbf{E}| = |c\mathbf{B}|$ as the impedance of free space requires. The length of the antenna arms is a critical parameter in this process. For appropriate values of λ/d, the geometric set-up ensures that the transient couples efficiently to the free-wave regime, so that the signal detaches from the antenna and propagates outward; for values poorly matched to the arm length, part of the energy remains bound to the structure, and the radiation efficiency is reduced.

The initial boundary value problem defined in this section is solved numerically in Section 6, which presents direct time-domain simulations of the full coupled system and demonstrates, in particular, the transition from the near-field regime, in which p and ρ_m are nonzero, to the free-wave regime characterizing the far field.

Numerical Scheme Adopted

The system (23)–(29) is discretized on a uniform two-dimensional grid in the cylindrical coordinates (r, z). We implement the Lax–Wendroff scheme [47] for the electromagnetic fields and an explicit upwind Euler method with artificial viscosity for the velocity part. The computational domain is the rectangle $[0, R_{\max}] \times [-Z_{\max}, Z_{\max}]$ in the (r, z)-plane, discretized with n_r grid points in the radial direction and n_z points in the axial direction:

$$r_i = i\,\Delta r, \quad i = 0, \ldots, n_r - 1, \qquad z_j = -Z_{\max} + j\,\Delta z, \quad j = 0, \ldots, n_z - 1, \tag{35}$$

with uniform spacings $\Delta r = R_{\max}/(n_r - 1)$ and $\Delta z = 2Z_{\max}/(n_z - 1)$. The axis of symmetry $r = 0$ coincides with the first grid column. The computational domain is chosen larger than the physical region of interest, so that a *sponge layer* technique (as explained in Section 7) can be applied without affecting the simulation in the vicinity of the antenna. This is done to avoid reverberation from the outflow boundary. The time step is chosen according to the Courant–Friedrichs–Lewy condition for the two-dimensional hyperbolic system

$$\Delta t = \nu \cdot \Delta t_{\max}, \qquad \Delta t_{\max} = \frac{\min(\Delta r, \Delta z)}{2\sqrt{2}\,c}, \tag{36}$$

where $\nu \in (0, 1]$ is a safety factor.

We first collect the three electromagnetic components into the vector $U = (E_1, B_2, E_3)$, so that the system (23)–(26) takes the form

$$\frac{\partial U}{\partial t} + A\,\frac{\partial U}{\partial r} + C\,\frac{\partial U}{\partial z} = P\,U, \tag{37}$$

with coefficient matrices

$$A = \begin{bmatrix} V_1 & 0 & 0 \\ 0 & 0 & -1 \\ V_3 & -c^2 & 0 \end{bmatrix}, \qquad C = \begin{bmatrix} 0 & c^2 & V_1 \\ 1 & 0 & 0 \\ 0 & 0 & V_3 \end{bmatrix}, \qquad P = \begin{bmatrix} -V_1/r & 0 & 0 \\ 0 & 0 & 0 \\ -V_3/r & c^2/r & 0 \end{bmatrix}. \tag{38}$$

The Lax–Wendroff update of (37) is constructed from a second-order Taylor expansion in time, with spatial derivatives approximated by centered differences. Denoting by $U^n_{i,j}$ the approximated solution at grid point (i, j) and time step n, and introducing the quantity $\lambda = \Delta t/h$ with $h = \min(\Delta r, \Delta z)$, the scheme reads

$$U^{n+1}_{i,j} = \left(I - \lambda^2\,(A^2 + C^2)\right)U^n_{i,j} + \mathcal{L}_r[U^n] + \mathcal{L}_z[U^n] + \mathcal{L}_{rz}[U^n] + \mathcal{S}[U^n], \tag{39}$$

where the operators on the right-hand side are defined as

$$\mathcal{L}_r[U] = \tfrac{1}{2}\lambda\,A\,(I + \lambda A)\,U_{i+1,j} - \tfrac{1}{2}\lambda\,A\,(I - \lambda A)\,U_{i-1,j}, \tag{40}$$

$$\mathcal{L}_z[U] = \tfrac{1}{2}\lambda\, C\,(I + \lambda C)\, U_{i,j+1} - \tfrac{1}{2}\lambda\, C\,(I - \lambda C)\, U_{i,j-1}, \tag{41}$$

$$\mathcal{L}_{rz}[U] = \frac{\lambda^2}{8}\,(AC + CA)\,\big(U_{i+1,j+1} + U_{i-1,j-1} - U_{i-1,j+1} - U_{i+1,j-1}\big). \tag{42}$$

The contribution, necessary to preserve second-order consistency in the presence of the $P\,U$ term in (37), is defined as

$$\begin{aligned}\mathcal{S}[U] = \Delta t\,\big(P + \tfrac{1}{2}\Delta t\, P^2\big)U_{i,j} &- \tfrac{1}{4}\lambda\,\Delta t\,(AP + PA)\,(U_{i+1,j} - U_{i-1,j}) \\ &- \tfrac{1}{4}\lambda\,\Delta t\,(CP + PC)\,(U_{i,j+1} - U_{i,j-1}).\end{aligned} \tag{43}$$

Formula (39) is applied at all interior grid points $1 \le i \le n_r - 2$, $1 \le j \le n_z - 2$.

Here follows the description of the algorithm: The pressure potential is advanced by a first-order explicit step applied directly to (24):

$$p_{i,j}^{n+1} = p_{i,j}^{n} + \Delta t\,\epsilon_0\,\rho_{i,j}^{n}\,\big(E_1^n\,V_1^n + E_3^n\,V_3^n\big)_{i,j}, \tag{44}$$

where the pseudocharge is recomputed at each time step from the current electromagnetic fields by finite-difference approximations of (23). The momentum equation is discretized in conservative form using the variables

$$M_1 = \rho_m V_1, \qquad M_3 = \rho_m V_3, \tag{45}$$

rather than the velocity components themselves. At each time step, the pseudomass is first advanced through an explicit discretization of the continuity Equation (29), namely,

$$\rho_m^{n+1} = \rho_m^n - \Delta t\,\nabla\cdot(\rho_m \mathbf{V})^n = \rho_m^n - \Delta t\,\nabla\cdot\mathbf{M}^n, \tag{46}$$

where $\mathbf{M} = (M_1, 0, M_3)$. On the antenna segment, the boundary condition (34) is imposed. The momentum variables are subsequently advanced as follows:

$$M_1^{n+1} = M_1^n - \Delta t\,(D_1^n + L_1^n + G_1^n),$$

$$M_3^{n+1} = M_3^n - \Delta t\,(D_3^n + L_3^n + G_3^n),$$

where for $k = 1, 3$, D_k^n collects the advective contributions, discretized by first-order upwind differences; L_k^n denotes the Lorentz forcing $-\epsilon_0\rho(\mathbf{E}^n + \mathbf{V}^n \times \mathbf{B}^n)_k$, evaluated pointwise; and G_k^n represents the pressure-gradient contribution $\partial_k p^n$, discretized by centered differences. Finally, the velocity field is recovered from

$$\mathbf{V}^{n+1} = \frac{\mathbf{M}^{n+1}}{\rho_m^{n+1}}, \tag{47}$$

whenever

$$|\rho_m^{n+1}| > \rho_{\mathrm{tol}},$$

where $\rho_{\mathrm{tol}} > 0$ is a prescribed positivity threshold. At grid points where the pseudomass falls below this threshold, the velocity field is left unchanged, in order to avoid division by values close to zero. This situation naturally occurs in the free-wave regime, where the pseudomass is zero while the velocity retains magnitude c.

There are two stabilization mechanisms applied during each time step. The first one is the exponential sponge layer applied in the annular region:

$$\{(r,z) : \sqrt{r^2 + z^2} > R_{\mathrm{sp}}\},$$

where $R_{\text{sp}} > 0$ is the sponge inner radius, as discussed in Section 7. The sponge suppresses reflections at the computational boundary by absorbing outgoing waves in the outer layer of cells. The second stabilization mechanism is a five-point isotropic diffusive filter. For the electromagnetic fields, the last computed values $F_{i,j}^{n+1}$, with $F = E_1, B_2, E_3$, are replaced by

$$F_{i,j}^{n+1} \leftarrow (1-\alpha)\, F_{i,j}^{n+1} + \frac{\alpha}{4}\left(F_{i+1,j}^{n+1} + F_{i-1,j}^{n+1} + F_{i,j+1}^{n+1} + F_{i,j-1}^{n+1}\right), \tag{48}$$

with $\alpha \in (0,1)$. A similar diffusive regularization is also applied to the variables p, V_1, V_3, with a possibly different diffusion parameter.

Boundary points are handled as follows: On the axis $r = 0$, Dirichlet boundary conditions are imposed as specified in some paragraphs above. On the three outer boundaries—right $(i = n_r)$, top $(j = n_z)$, and bottom $(j = 1)$—approximate characteristic boundary corrections are applied to the electromagnetic subsystem. These corrections are based on the characteristic structure associated with the propagation speeds $V_1 \pm c$ on the radial boundary and $V_3 \pm c$ on the upper and lower boundaries. One-sided finite differences are used in the normal direction.

6. Results

We show the results of an experiment employing the scheme described in Section 5. The simulations were performed using the following parameters, which are intended to be academic, without going into the engineering details of a real device. Of course, in the presence of realistic data, the experiment could be reproduced without major difficulties. The speed of light, the antenna length, and the vacuum permittivity are normalized to $c = 1$, $d = 1$, and $\epsilon_0 = 1$, respectively. The computational domain is $[0, R_{\max}] \times [-Z_{\max}, Z_{\max}]$, with $R_{\max} = 6$ and $Z_{\max} = 6$, and is discretized by $n_r = 121$ and $n_z = 241$ uniformly spaced grid points. This yields the mesh sizes $\Delta r = R_{\max}/(n_r - 1) = 0.05$ and $\Delta z = 2Z_{\max}/(n_z - 1) = 0.05$. The time step satisfies the CFL condition

$$\Delta t = \nu\, \Delta t_{\max}, \qquad \Delta t_{\max} = \frac{\min(\Delta r, \Delta z)}{2\sqrt{2}\, c},$$

with safety factor $\nu = 0.1$, giving $\Delta t \simeq 1.77 \times 10^{-3}$. The simulations were carried out up to the final time $T = 5$.

The pseudomass prescribed on the antenna satisfies $\rho_m = M_q\, \epsilon_0\, |\rho|$. In the simulations, the normalization $M_q\, \epsilon_0 = 1$ was adopted, so that the imposed boundary condition simply became $\rho_m = |\rho|$. This choice is certainly unrealistic. In fact, we expect $M_q\, \epsilon_0$ to be very small, given that the contribution of pseudomass should play a minimal role in evolution. However, this allows us to better observe the dynamic behavior of the velocity field. The threshold used for the recovery of the velocity field was $\rho_{\text{tol}} = 10^{-1}$, so that the velocity was updated only where $|\rho_m| > \rho_{\text{tol}}$.

Numerical stabilization was provided by two complementary mechanisms. The electromagnetic fields were regularized through the five-point diffusive filter described in Section 5 using the diffusion coefficient $\alpha_{\text{EM}} = 0.10$, whereas the variables (p, V_1, V_3) were regularized by an explicit Laplacian diffusion step with $\alpha_{\text{mech}} = 0.05$. Finally, outgoing waves were absorbed by an exponential sponge layer occupying the outer $n_{\text{sponge}} = 8$ grid cells, corresponding to $R_{\text{sp}} = R_{\max} - n_{\text{sponge}} \Delta r$, with damping coefficient $\sigma_{\max} = 8/\Delta t$.

In Figure 3, we give some snapshots of the evolution of the electric field. Remember that the source is not pointwise. The signal actually emerges by following the contours of the antenna. The evolution at a certain distance coincides with what is expected from a spherical wave, and this concerns both the electric and magnetic fields to the same extent. It is important to note that what is shown is not only the behavior of the periodic regime but also includes a transient period in which the wave tends to settle. In fact, the device is not powered at the beginning. Consequently, both the electric and magnetic fields are initially zero. In this simulation, we chose $\tau = 0$ in (32), so $\mathbf{B}$ continued to remain zero at the boundary and, therefore, out of phase with respect to the $\mathbf{E}$ there. Miraculously, the fields found themselves in phase a short distance from the emitter, exactly reproducing the behavior of a free wave. We can realize this property by examining the one-dimensional graphs of Figure 4, where the electric and magnetic fields on the axis $z = 0$ are reported. As can clearly be seen, $\mathbf{E}$ and $\mathbf{B}$ are completely out of phase near the origin, but they quickly find a perfect harmony as they move away. As expected, their intensity damps with the distance. To evidentiate this behavior, we also plotted in Figure 4 the quantity $|\mathbf{E} + \mathbf{V} \times \mathbf{B}|$, which is equivalent to $\big||\mathbf{E}| - |c\mathbf{B}|\big|$ when $\mathbf{E} \cdot \mathbf{V} = 0$ and $|\mathbf{V}| = c$. This tends to decay far from the source, confirming that the wave is actually transverse and follows the rules of geometrical optics.

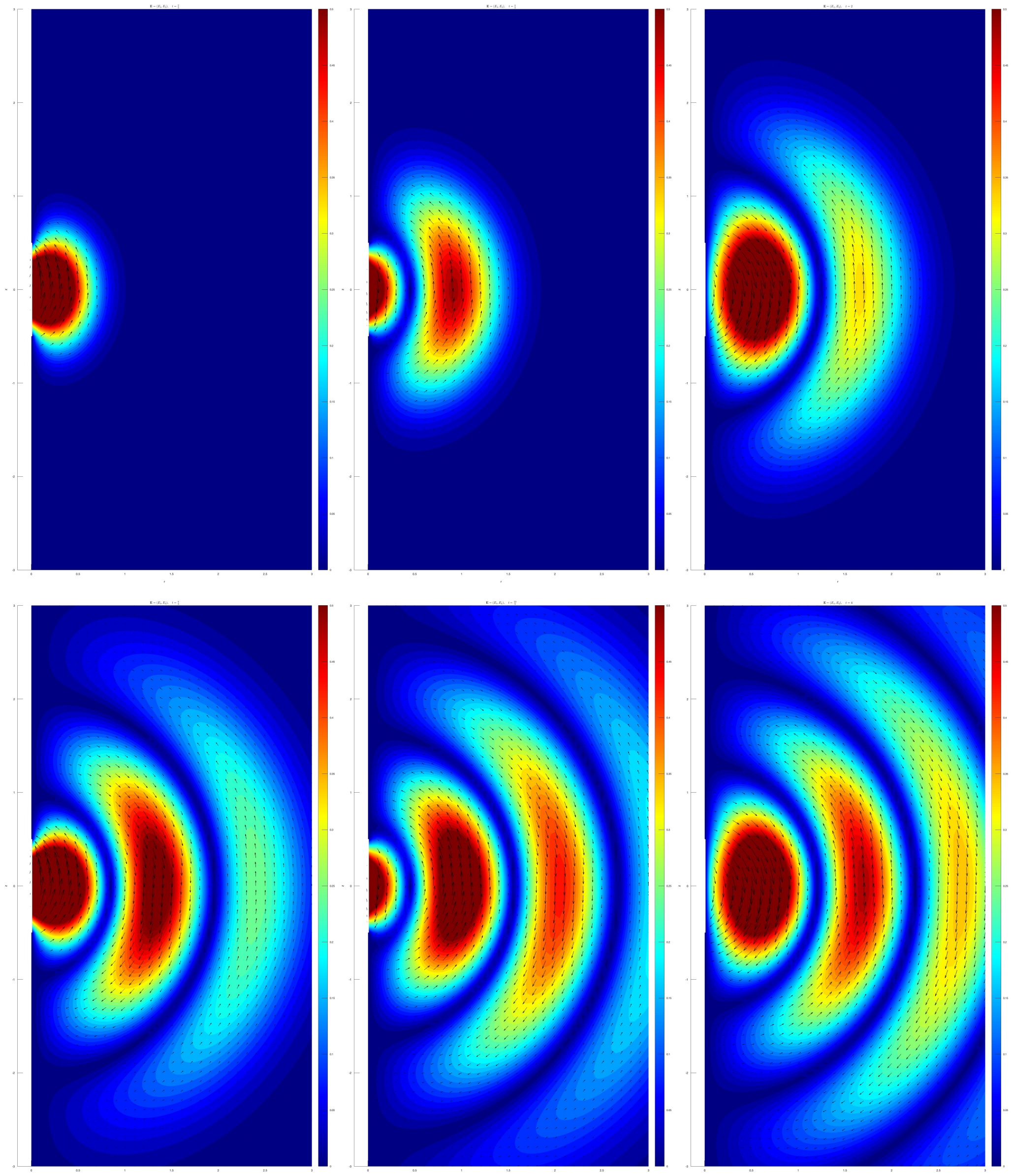

Figure 3. Snapshots of the electric field magnitude $|\mathbf{E}|$ superimposed on the arrow plots (E_1, E_3), at times $t = 0.66, 1.33, 2.0, 2.66, 3.33, 4.0$.

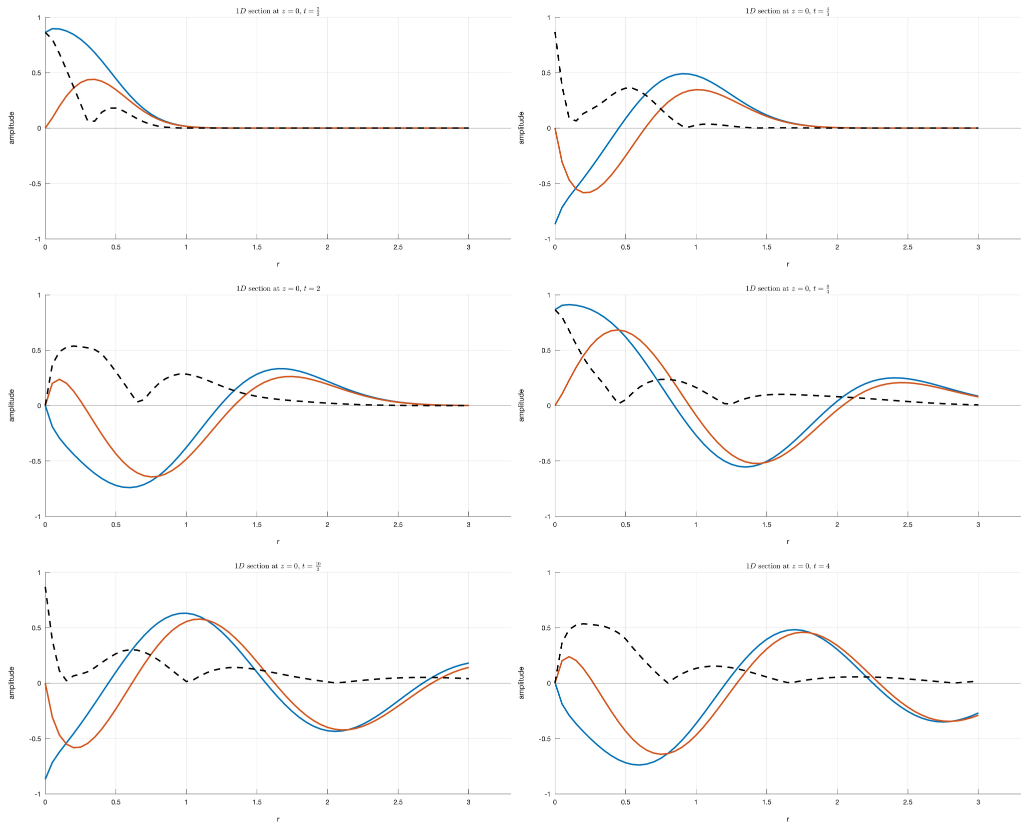

Figure 4. One-dimensional sections of the fields at $z = 0$ for times $t = 0.66, 1.33, 2.0, 2.66, 3.33, 4.0$. We can see the intensity of the vertical component of the electric field E_3 (blue graph) and that of $-B_2$ (red graph; the sign has been switched to emphasize the fact that the electric and magnetic fields assume the same phase at a distance from the source). Moreover, we report the quantity $|\mathbf{E} + \mathbf{V} \times \mathbf{B}|$ (black dashed line). In the initial moments, at the the far right, this last quantity is exactly zero, since the wave has not yet reached the final point. Later, it becomes different from zero, albeit remaining rather small. By enlarging the computational domain, we expect the phasing to be completed at some distance.

Figure 5 shows the distributions of the pseudocharge ρ (left), the pseudomass ρ_m (center), and the pressure field p (right) at time $t = 4$. Both ρ_m and p are only relevant in the neighborhood of the antenna, where they are meaningful in the near- to far-field transition process. The pseudocharge ρ takes positive and negative values with zero average (see the reinterpretation of the Gauss theorem given in (49)). From the theoretical viewpoint, it is never equal to zero, but the magnitude decreases as $1/r^2$, so it can actually be confused with a free-divergence Maxwellian wave. In this regime, the entire set of equations becomes linear and reflects the behavior of standard electrodynamics. This confirms once again that what is proposed here is an extension of the usual model that is not in conflict with already-known notions.

Finally, we can say something about the behavior of the velocity field (see also Figure 2). This does not stabilize at a constant displacement but continues to oscillate slightly in a neighborhood of the antenna, following the periodicity of the signal. This behavior is more or less evident depending on how the various parameters are set. At a distance from the source, where ρ_m and p are zero, $\mathbf{V}$ is not modified, thus indicating the direction of the rays of a spherical wave that propagates respecting Huygens' principle.

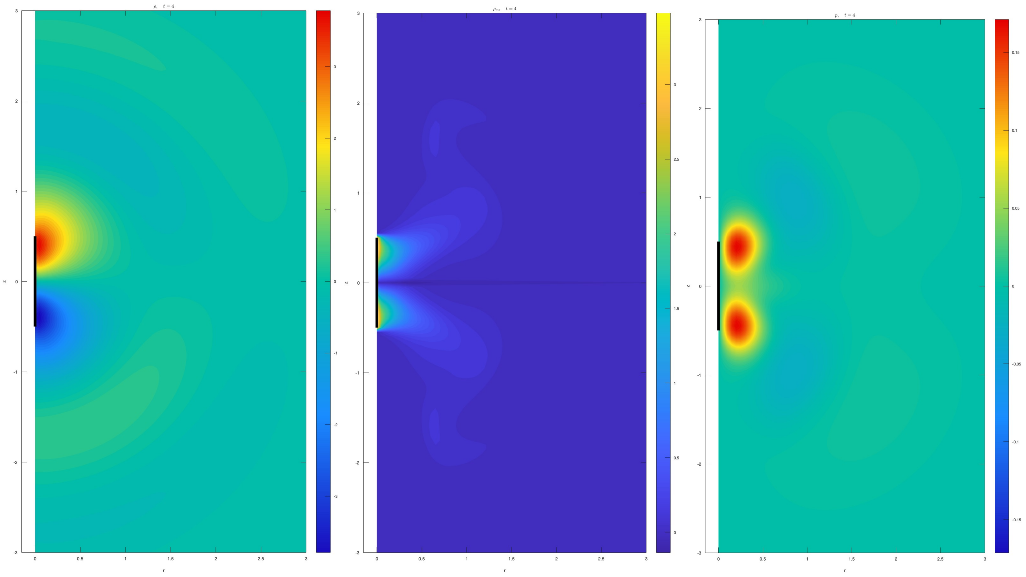

Figure 5. Distribution of the pseudocharge ρ (**left**), the pseudomass ρ_m (**center**), and the pressure p (**right**) at time $t = 4$. The last two quantities are confined in a neighborhood of the antenna and are practically zero away from the source, indicating the transition from the near-field dynamics to the free-wave regime.

Further numerical data are not significant for the validation of the model, as they are strictly linked to the numerical techniques used. By its construction, the model ensures the conservation of energy and pseudocharge; however, the choice of the discretization parameters h, Δt, and the parameters related to artificial diffusion does not allow a perfect preservation of these quantities. As reiterated several times in this article, the choice of the numerical method is marginal. We are not, in fact, proposing a specific technique for a given problem; we simply chose one of the most popular ones to verify the capabilities of the physical model. Other experiments, not reported here, where the frequency is varied with respect to the length of the dipole, confirm what is already known about the behavior of radio signal emission. On the other hand, the purpose of this paper is not to provide a broad case history but to give the preliminary basis for more serious simulations to be carried out in the future on known, or less known, devices.

7. Further Remarks

In Section 2, we introduced the extended system (2)–(4) recovered from conservation arguments. The scalar $\rho = \nabla \cdot \mathbf{E}$ acquires the role of a charge-like density, called pseudocharge. The auxiliary velocity field $\mathbf{V}$ is understood as the local carrier of electromagnetic information, ρ_m is identified with a sort of mass-like density, and the scalar p tracks the exchange between bound and radiating energy during transients. In the classical formulation (13), the scalar $\nabla \cdot \mathbf{E}$ vanishes in every source-free region, and the presence of any nonzero divergence of the electric field is unambiguously associated with a physical charge distribution. The extended system (2)–(4) relaxes this identification: the quantity ρ defined in (1) may be locally nonzero in regions where no real charges are present, with its evolution governed by the conservation law (5) and its effect on the electromagnetic fields entering through the $\rho\mathbf{V}$ term in (2). Actually, the quantity $\rho\mathbf{V}$ plays the role of an effective current density in the Ampère equation. The three elementary configurations of Figure 1 illustrate why the extended formulation is a natural rather than exceptional feature of electromagnetic radiation. In each of these three cases, a direct calculation shows that no choice of the electromagnetic fields satisfies $\nabla \cdot \mathbf{E} = 0$ in the source-free region. Conversely, each admits a solution of the extended system (2)–(4) in which ρ is locally nonzero but globally neutral, as made precise below.

A simple Gauss-type result states that the pseudocharge integrates to zero over the transverse support of a free wave. This result is consistent with the empirical content of Gauss's law at the macroscopic level. We check it here in the case of the spherical wave. A direct computation of $\rho = \nabla \cdot \mathbf{E}$ from the field expression (19) yields the following for any f and any g:

$$\rho = \frac{1}{r^2 \sin\theta} \frac{\partial}{\partial\theta}\big(f(\theta)\sin\theta\big)\, g(ct - r).$$

Using $r^2 \sin\theta$ as the Jacobian in spherical coordinates (r, θ, ϕ), the volume integral factorizes as

$$\int_\Omega \rho\, dV = 2\pi \int_I \left(\int_0^\pi \frac{\partial}{\partial\theta}\big(f(\theta)\sin\theta\big)\, d\theta \right) g(ct - r)\, dr = 0, \tag{49}$$

for any time t, where $\Omega = I \times [0, \pi] \times [0, 2\pi]$ and I is any interval in the radial direction. The inner integral evaluates to $\big[f(\theta)\sin\theta\big]_0^\pi = 0$, regardless of f, which proves the claim. The result has a direct physical reading. A localized free-wave packet may carry nonzero charge-like density at every point of its support, but the total density enclosed in any spherical shell vanishes. The role of the pseudocharge is to allow the local configuration of the fields some additional flexibility compared with a totally free-divergence constraint.

The auxiliary field $\mathbf{V}$ is interpreted as the local carrier of electromagnetic information: at each point, it indicates the direction along which the signal is propagating. For free waves, one finds that $|\mathbf{V}| = c$ holds pointwise and $\mathbf{V}$ aligns with the Poynting vector $\mathbf{E} \times \mathbf{B}$. Outside the free-wave regime, when ρ_m or p is nonzero, $\mathbf{V}$ is not requested to preserve the magnitude or remain aligned with the Poynting vector. Its evolution is governed by the Euler-type equation in (3), coupled to the electromagnetic fields through the Lorentz-type forcing $\epsilon_0 \rho(\mathbf{E} + \mathbf{V} \times \mathbf{B})$. The distinction between the electromagnetic information and the carrier that transports it is a structural feature of the model: it is the velocity field that carries the optics content, while the electromagnetic fields $\mathbf{E}$ and $\mathbf{B}$ record the physical observable.

The scalar ρ_m plays a role analogous to that of a fluid mass density in classical continuum mechanics. In principle, ρ_m may also be locally nonzero in regions where no material carriers are present. In the applications, the continuity equation has been replaced by a direct constitutive relation between ρ_m and ρ, namely, $\rho_m = M_q \epsilon_0 |\rho|$. This setting is a constitutive choice, motivated by some considerations: First, the absolute value in (34) guarantees the positivity of ρ_m, consistent with its interpretation as a mass density. Second, this form of closure is continuous with the identification proposed in [31,32] between ρ_m and the rest-mass density of elementary charged particles in the subatomic regime. In that context, the coefficient M_q is identified with the ratio between the electron rest mass and the unitary elementary charge, which makes $M_q \epsilon_0$ extremely small. In the antenna regime considered in the present paper, the parameter M_q is treated as a free modeling coefficient, and the equality $\rho_m = M_q\, \epsilon_0\, |\rho|$ is only imposed at the boundary.

More generally, the coefficients of the model (such as the ratio λ/d between wavelength and antenna length, the reflection parameter τ, and the coefficient M_q, as well as the relative permittivity ϵ_r, the relative magnetic permeability μ_r, the internal resistance of the conducting wires, etc.) can be freely chosen, so that the framework is not tied to a specific device but describes a whole class of dipole configurations. For this reason, the simulations are reported in normalized units. In fact, the aim here is to establish the model, not to design a particular antenna. We have checked (and the experiments are not reported here for simplicity) that when the frequency is not matched to the antenna length, all of the familiar behaviors of the classical dipole appear, including radiation efficiency and directivity. A complete case study, reporting engineering figures of merit, is a natural application of the framework but is outside of the scope of the present work. This generality is not limited to varying the parameters of a single dipole. Being formulated at the level of the governing equations, the model can be addressed to the study of other radiating structures. In principle, even antenna arrays, for example, can be accommodated through an appropriate specification of the source and boundary data.

The scalar p evolves through (4) with a source $\epsilon_0\,\rho\,\mathbf{E}\cdot\mathbf{V}$. In a free-wave regime, the orthogonality of the triplet $(\mathbf{E},\mathbf{B},\mathbf{V})$ ensures that $\mathbf{E}\cdot\mathbf{V}=0$. Setting $p=0$ in such a regime is therefore consistent with the equations. Outside the free-wave regime, $\mathbf{E}\cdot\mathbf{V}$ may be nonzero, and p evolves as a scalar potential tracking the local exchange between electromagnetic and mechanical energy. Two situations in which this exchange is physically significant deserve mention: The first is the near-field region of an emitting antenna, in which the electromagnetic fields are still bound to the feeding geometry, and the orthogonality of $(\mathbf{E},\mathbf{B},\mathbf{V})$ is broken. The scalar p is nonzero there. The second is the exterior of a time-varying charge distribution whose emission is purely longitudinal (the third configuration in Figure 1). Radiation pressure [48,49] and related phenomena, in which electromagnetic energy is converted into mechanical energy upon interaction with matter, are naturally accommodated within this framework. In terms of energy, the extended formulation suggests a natural scalar combination of electromagnetic, kinetic, and potential contributions:

$$\mathcal{T}=\rho_m\,c^2-\tfrac{1}{2}\epsilon_0\left(|\mathbf{E}|^2+c^2|\mathbf{B}|^2\right)-p. \tag{50}$$

In a pure free-wave regime, where $\rho_m=0$ and $p=0$, $\mathcal{T}$ reduces to the (minus) classical electromagnetic energy density $\mathcal{E}$.

The boundary condition $B_2=(\tau/c)\,E_3$ adopted in Section 5 is closely related to a body of classical work on the electromagnetic boundary conditions at conductor surfaces. The question has received a systematic treatment in the engineering and applied physics literature. Maxwell himself (pp. 161–175, 281–512, [38]) and ref. [39] provided some foundational results. Heaviside [37] extended this framework through an analysis of the energy current along a conductor. J. J. Thomson [50], examined moving fields at conductor surfaces in detail. A quantitative treatment of the boundary condition on a conductor of finite conductivity at fixed frequency was developed in the 1940s. The Shchukin–Leontovich impedance boundary condition was introduced in [51]. The underlying asymptotic derivation, based on the smallness of the skin depth compared to the surface radius of curvature, appeared earlier in [52]. A comprehensive modern treatment covering the full hierarchy of approximate boundary conditions, together with rigorous error estimates, is given in [53]. The Shchukin–Leontovich condition is also discussed in the standard textbook treatment of macroscopic electrodynamics [54]. Other related references are [55–59]. The impedance-type boundary condition (32) used in the present paper falls within the Shchukin–Leontovich surface impedance tradition. Here, the condition is formulated directly in the time domain, with a real constant τ rather than a frequency-dependent complex impedance.

Since a numerical solver must work on a bounded computational domain, the truncation of the physical domain to a finite box introduces the possibility of spurious reflections at the artificial boundary that propagate back toward the antenna and contaminate the solution in the "region of interest". This difficulty is addressed here through the combination of two strategies: an enlarged computational domain, and an absorbing layer, the sponge, applied in the outer portion of the computational domain, which damps outgoing signals before they reach the farther boundary. Thus, the actual computational domain on which the numerical scheme operates is chosen strictly larger than the region of interest. Inside the sponge region $\{\sqrt{r^2+z^2} > R_{\rm sp}\}$, where $R_{\rm sp}$ is given, each field is damped multiplicatively at every time step:

$$F_{i,j}^{n+1} \leftarrow F_{i,j}^{n+1} \exp\bigl(-\sigma(r_i, z_j)\,\Delta t\bigr), \qquad \sigma(r,z) = \sigma_{\max}\left(\frac{\sqrt{r^2+z^2} - R_{\rm sp}}{R_{\rm dom} - R_{\rm sp}}\right)^2, \tag{51}$$

where $R_{\rm dom} = \sqrt{R_{\max}^2 + Z_{\max}^2}$ and $\sigma_{\max}$ is a given coefficient. A wave entering the sponge experiences a gradually increasing absorption rather than a sudden step. The sponge layer is closely related to the absorbing-layer strategies widely used in computational electromagnetics and fluid dynamics [60–62].

8. Conclusions

The dipole antenna, despite its long history, still poses modeling challenges in the near-field region, where a bound signal detaches from the conductor and becomes a freely propagating wave. The vacuum Maxwell–Heaviside system supplies too few configurations to describe this transient, since exact outgoing waves compatible with geometrical optics need not to satisfy $\nabla \cdot \mathbf{E} = 0$. We have addressed this by extending the model with an auxiliary velocity field $\mathbf{V}$, a pseudocharge $\rho = \nabla \cdot \mathbf{E}$, a pseudomass ρ_m, and a pressure-like potential p, so that the outgoing signal is treated as an electromagnetic fluid carrying a charge-like density. In the far field, the extended system (2)–(4) reduces to an exact family of spherical free-wave solutions obeying the rules of geometrical optics, as presented in Section 4. The near-to-far transition acquires a concrete dynamical description: the pressure-like potential p tracks the conversion between bound and radiating energy and vanishes once the wave propagates freely.

A distinctive feature of the approach is that the nonlinear system is integrated directly in time, without solving wave equations or computing eigenfunctions. The divergence and charge-conservation conditions are respected by construction rather than imposed as external constraints that the evolution may subsequently violate. Eigenfunction expansions, such as the one leading to the Hertz solutions (16), satisfy the vanishing-divergence conditions in vacuum but are poorly suited to the region close to the antenna, where $\nabla \cdot \mathbf{E}$ cannot be expected to vanish.

From a physical standpoint, a large amount of energy is generated almost pointwise in the small gap between the two arms, and it remains bound to the conductor until the signal is completely released. The arm length governs how cleanly this detachment occurs. The potential p enforces the conservation of total energy (see (50)): it is nonzero during the transition, when $\mathbf{B}$ is still developing and out of phase with respect to $\mathbf{E}$, and vanishes once the wave carries all of its energy freely. Upon impact with a physical body, such a wave can perform work by converting part of its electromagnetic energy into mechanical energy, which lays a foundation for relating electrodynamics to Newtonian forces, albeit through possibly very small conversion factors [15,48]. One of the most important features is that the device is initially turned off and is successively activated by a signal. This means that both the time transient and asymptotic periodic behavior of the generated wave are simulated, and this represents an improvement over the most commonly used approaches.

The framework has been illustrated on a standard dipole antenna through direct time-domain simulation of the full coupled system, suggesting a unified analytical and computational pathway for antenna modeling.

Author Contributions: Conceptualization, D.F.; methodology, D.F., L.F., G.M.; software, L.F., G.M.; writing—review and editing, D.F., L.F., G.M. All authors have read and agreed to the published version of the manuscript.

Funding: This research received no external funding.

Institutional Review Board Statement: Not applicable.

Informed Consent Statement: Not applicable.

Data Availability Statement: The data and source code supporting the numerical experiments reported in this manuscript are available from the corresponding author upon reasonable request.

Acknowledgments: All of the authors are affiliated with GNCS-INdAM, the Italian Gruppo Nazionale per il Calcolo Scientifico, Istituto Nazionale di Alta Matematica. During the preparation of this manuscript, the authors used AI-based assistants for writing and editing support; the authors have reviewed and edited the output and take full responsibility for the content of this publication.

Conflicts of Interest: The authors declare no conflicts of interest.

References

1. Balanis, C.A. *Antenna Theory: Analysis and Design*, 3rd ed.; John Wiley & Sons: Hoboken, NJ, USA, 2005.
2. Jackson, J.D. *Classical Electrodynamics*, 2nd ed.; John Wiley & Sons: New York, NY, USA, 1975.
3. Wang, C.; Xu, H.X.; Zhu, R.; Ding, H.; Li, B.; Wang, X.; Yang, C.; Lu, Y. 3-D-Printed Pentahedral Polarization-Division Transmissive Metadevice With Versatile Wavefronts. *IEEE Trans. Antennas Propag.* **2026**, *74*, 4915–4920. [CrossRef]
4. Zou, X.J.; Wang, Y.W.; Zong, B.F.; Xu, X.G.; Han, L.X.; Zhu, H.; Song, W.; Tan, M.; Du, H.N. Miniaturized Low-Profile Ultrawideband Antipodal Vivaldi Antenna Array Loaded With Edge Techniques. *IEEE Trans. Antennas Propag.* **2026**, *74*, 1156–1161. [CrossRef]
5. Liu, T.; Chen, H.; Wang, W.; Sun, H.; Hu, L.; Chen, M.; Chu, Z.; Xu, K.; Wang, B.; Wang, L.; et al. Multispectral compatible stealth programmable coding metasurface with independent and dynamic manipulation of absorption and scattering. *Photonics Res.* **2026**, *14*, 2646–2658. [CrossRef]
6. Gas, P.; Miaskowski, A. SAR Optimization for Multi-Dipole Antenna Array with Regard to Local Hyperthermia. *Prz. Elektrotech.* **2019**, *95*, 17–20. [CrossRef]
7. Gas, P.; Miaskowski, A.; Subramanian, M. In Silico Study on Tumor-Size-Dependent Thermal Profiles inside an Anthropomorphic Female Breast Phantom Subjected to Multi-Dipole Antenna Array. *Int. J. Mol. Sci.* **2020**, *21*, 8597. [CrossRef] [PubMed]
8. EZNEC. Available online: https://www.eznec.com/ (accessed on 14 August 2026).
9. GAL-ANA. Available online: http://gal-ana.de/basicmm/en/ (accessed on 14 August 2026).
10. Born, M.; Wolf, E. *Principles of Optics: Electromagnetic Theory of Propagation, Interference and Diffraction of Light*, 6th ed.; Pergamon Press: Oxford, UK, 1980.
11. Jackson, J.D. How an antenna launches its input power into radiation: The pattern of the Poynting vector at and near an antenna. *Am. J. Phys.* **2006**, *74*, 280–288. [CrossRef]
12. McDonald, K.T. *Radiation in the Near Zone of a Center-Fed Linear Antenna*; Technical report; Princeton University: Princeton, NJ, USA, 2004. Available online: https://kirkmcd.princeton.edu/examples/linearantenna.pdf (accessed on 14 August 2026)
13. Funaro, D. Truths and Myths About the Equations of Electrodynamics. 2025, *Preprint*. Available online: https://hal.science/hal-04902347v1 (accessed on 14 August 2026).
14. Funaro, D. Numerical Simulation of Electromagnetic Solitons and their Interaction with Matter. *J. Sci. Comput.* **2010**, *45*, 259. [CrossRef]
15. Funaro, D.; Kashdan, E. Simulation of Electromagnetic Scattering with Stationary or Accelerating Targets. *Int. J. Mod. Phys. C* **2015**, *26*, 1–16. [CrossRef]
16. Ashkin, A. Acceleration and Trapping of Particles by Radiation Pressure. *Phys. Rev. Lett.* **1970**, *24*, 156–159. [CrossRef]
17. Ashkin, A.; Dziedzic, J.M.; Bjorkholm, J.E.; Chu, S. Observation of a single-beam gradient force optical trap for dielectric particles. *Opt. Lett.* **1986**, *11*, 288–290. [CrossRef] [PubMed]
18. Ashkin, A.; Dziedzic, J.M. Optical Trapping and Manipulation of Viruses and Bacteria. *Science* **1987**, *235*, 1517–1520. [CrossRef] [PubMed]
19. Ashkin, A.; Dziedzic, J.M.; Yamane, T. Optical Trapping and Manipulation of Single Cells Using Infrared Laser Beams. *Nature* **1987**, *330*, 769–771. [CrossRef] [PubMed]
20. Svoboda, K.; Block, S.M. Biological Applications of Optical Forces. *Annu. Rev. Biophys. Biomol. Struct.* **1994**, *23*, 247–285. [CrossRef] [PubMed]
21. He, H.; Friese, M.E.J.; Heckenberg, N.R.; Rubinsztein-Dunlop, H. Direct Observation of Transfer of Angular Momentum to Absorptive Particles from a Laser Beam with a Phase Singularity. *Phys. Rev. Lett.* **1995**, *75*, 826–829. [CrossRef] [PubMed]
22. Padgett, M.; Bowman, R. Tweezers with a Twist. *Nat. Photonics* **2011**, *5*, 343–348. [CrossRef]

23. Maragò, O.M.; Jones, P.H.; Gucciardi, P.G.; Volpe, G.; Ferrari, A.C. Optical Trapping and Manipulation of Nanostructures. *Nat. Nanotechnol.* **2013**, *8*, 807–819. [CrossRef] [PubMed]
24. Gosse, C.; Croquette, V. Magnetic Tweezers: Micromanipulation and Force Measurement at the Molecular Level. *Biophys. J.* **2002**, *82*, 3314–3329. [CrossRef] [PubMed]
25. Grier, D.G. A Revolution in Optical Manipulation. *Nature* **2003**, *424*, 810–816. [CrossRef] [PubMed]
26. Neuman, K.C.; Block, S.M. Optical Trapping. *Rev. Sci. Instrum.* **2004**, *75*, 2787–2809. [CrossRef] [PubMed]
27. Neuman, K.C.; Nagy, A. Single-molecule force spectroscopy: Optical tweezers, magnetic tweezers and atomic force microscopy. *Nat. Methods* **2008**, *5*, 491–505. [CrossRef] [PubMed]
28. Jeffrey, A. *Magnetohydrodynamics*; Oliver & Boyd: Edinburgh, UK, 1966.
29. Davidson, P.A. *An Introduction to Magnetohydrodynamics*; Oxford University Press: London, UK, 2001.
30. Molokov, S.S.; Moreau, R.; Moffatt, H.K. (Eds.) *Magnetohydrodynamics: Historical Evolution and Trends*; Springer: Berlin/Heidelberg, Germany, 2007.
31. Funaro, D. *Electromagnetism and the Structure of Matter*; World Scientific: Singapore, 2008.
32. Funaro, D. *From Photons to Atoms, the Electromagnetic Nature of Matter*; World Scientific: Singapore, 2019.
33. Chiolerio, A.; Diazzi, L.; Funaro, D. Highly Directive Biconic Antennas Embedded in a Dielectric. *Appl. Sci.* **2020**, *10*, 8828. [CrossRef]
34. Funaro, D.; Chiolerio, A. Tests on High-Directivity Unconventional Biconical Type Antennas. *arXiv* **2022**, arXiv:2202.01887.
35. Fock, V. *The Theory of Space, Time and Gravitation*; Pergamon Press: London, UK, 1959.
36. Misner, C.W.; Thorne, K.S.; Wheeler, J.A. *Gravitation*; W. H. Freeman & c.: San Francisco, CA, USA, 1973.
37. Heaviside, O. On the forces, stresses and fluxes of energy in the electromagnetic field. *Philos. Trans. R. Soc.* **1893**, *183A*, 423. [CrossRef]
38. Maxwell, J.C. On physical lines of force. *Lond. Edinb. Dublin Philos. Mag. J. Sci.* **1861**, *21*, 281–291. [CrossRef]
39. Maxwell, J.C. A dynamical theory of the electromagnetic field. *Philos. Trans. R. Soc. Lond.* **1865**, *165*, 459–512. [CrossRef]
40. Hertz, H. The forces of the electric oscillations treated according to Maxwell's theory. *Nature* **1889**, *39*, 402–404, 450–452. [CrossRef]
41. Hertz, H. *Electric Waves*; Dover: New York, NY, USA, 1962.
42. Joos, G. *Theoretical Physics*, 3rd ed.; Dover Pub.: New York, NY, USA, 1986.
43. Funaro, D. The space-time outside a pulsating charged sphere. *Appl. Sci.* **2022**, *12*, 7290. [CrossRef]
44. Anderson, L.I. *Nikola Tesla on His Work With Alternating Currents and Their Application to Wireless Telegraphy, Telephony, and Transmission of Power*; Sun Publishing: Denver, CO, USA, 1992.
45. Damm, G.W. The Tesla longitudinal wave. *Electr. Spacecr. J.* **1995**, *15*, 23–26.
46. Smoller, J. *Shock Waves and Reaction-Diffusion Equations*, 2nd ed.; Grundlehren der mathematischen Wissenschaften; Springer: New York, NY, USA, 1994; Volume 258.
47. Lax, P.D.; Wendroff, B. Systems of Conservation Laws. *Commun. Pure Appl. Math.* **1960**, *13*, 217–237. [CrossRef]
48. Funaro, D. Newtonian Forces Exerted by Electromagnetic Waves Traveling into Matter. *Int. J. Theor. Phys.* **2023**, *62*, 231. [CrossRef]
49. Cohen-Tannoudji, C.N. Manipulating atoms with photons. *Rev. Mod. Phys.* **1998**, *70*, 707. [CrossRef]
50. Thomson, J.J. *Notes on Recent Researches in Electricity and Magnetism, Intended as a Sequel to Professor Clerk-Maxwell's Treatise on Electricity and Magnetism*; Clarendon Press: Oxford, UK, 1893.
51. Leontovich, M.A. On the Approximate Boundary Conditions for the Electromagnetic Field on the Surface of Well-Conducting Bodies. In *Investigations on Propagation of Radio Waves*; Vvedenskii, B.A., Ed.; Academy of Sciences USSR: Moscow, Russia, 1948; pp. 5–10. (In Russian)
52. Rytov, S.M. Calculation of the Skin Effect by the Perturbation Method. *Zhurnal Eksp. Teor. Fiz.* **1940**, *10*, 180–190. (In Russian)
53. Senior, T.B.A.; Volakis, J.L. *Approximate Boundary Conditions in Electromagnetics*; Institution of Electrical Engineers: London, UK, 1995.
54. Landau, L.D.; Lifshitz, E.M. *Electrodynamics of Continuous Media*, 2nd ed.; Pergamon Press: Oxford, UK, 1984; Volume 8 of Course of Theoretical Physics.
55. Pocklington, H.C. Electrical Oscillations in Wires. *Proc. Camb. Philos. Soc.* **1897**, *9*, 324–332.
56. Hallén, E. Theoretical Investigations into the Transmitting and Receiving Qualities of Antennae. *Nova Acta Regiae Soc. Sci. Ups.* **1938**, *11*, 1–44.
57. Schelkunoff, S.A. *Advanced Antenna Theory*; John Wiley & Sons: New York, NY, USA, 1952.
58. King, R.W.P. *The Theory of Linear Antennas*; Harvard University Press: Cambridge, MA, USA, 1956.
59. Sommerfeld, A. Über die Ausbreitung der Wellen in der drahtlosen Telegraphie. *Ann. Phys.* **1909**, *333*, 665–736. [CrossRef]
60. Berenger, J.P. A perfectly matched layer for the absorption of electromagnetic waves. *J. Comput. Phys.* **1994**, *114*, 185–200. [CrossRef]

https://doi.org/10.3390/app16168334

61. Colonius, T. Modeling artificial boundary conditions for compressible flow. *Annu. Rev. Fluid Mech.* **2004**, *36*, 315–345. [CrossRef]
62. Israeli, M.; Orszag, S.A. Approximation of radiation boundary conditions. *J. Comput. Phys.* **1981**, *41*, 115–135. [CrossRef]

https://doi.org/10.3390/app16168334